Applied Physics Reviews

RESEARCH ARTICLE | APRIL 30 2024

Demystifying metal-assisted chemical etching of GaN and related heterojunctions

Clarence Y. Chan ; Jan Paul Menzel ; Yicong Dong ; Zhuoran Long ; Aadil Waseem ; Xihang Wu ; Yixin Xiao ; Jinqiao Xie ; Edmond K. C. Chow ; Shaloo Rakheja ; Victor S. Batista ; Zetian Mi ; Xiuling Li

Appl. Phys. Rev. 11, 021416 (2024)
https://doi.org/10.1063/5.0186709

30 April 2024 15:54:17

Applied Physics Reviews ARTICLE pubs.aip.org/aip/are

Demystifying metal-assisted chemical etching of GaN and related heterojunctions

Cite as: Appl. Phys. Rev. **11**, 021416 (2024); doi: 10.1063/5.0186709
Submitted: 8 November 2023 · Accepted: 5 April 2024 ·
Published Online: 30 April 2024

Clarence Y. Chan,[1] Jan Paul Menzel,[2] Yicong Dong,[1] Zhuoran Long,[2] Aadil Waseem,[3] Xihang Wu,[3] Yixin Xiao,[4] Jinqiao Xie,[5] Edmond K. C. Chow,[1] Shaloo Rakheja,[1] Victor S. Batista,[2] Zetian Mi,[4] and Xiuling Li[1,3,a)]

AFFILIATIONS

[1]Department of Electrical and Computer Engineering, Holonyak Micro and Nanotechnology Laboratory, University of Illinois at Urbana-Champaign, Urbana, Illinois 61801, USA
[2]Department of Chemistry, Yale University, New Haven, Connecticut 06520, USA
[3]Department of Electrical and Computer Engineering, Microelectronics Research Center, The University of Texas, Austin, Texas 78758, USA
[4]Department of Electrical Engineering and Computer Science, University of Michigan, Ann Arbor, Michigan 48109, USA
[5]Qorvo, Richardson, Texas 75080, USA

[a)]Author to whom correspondence should be addressed: xiuling.li@utexas.edu

ABSTRACT

GaN and related semiconductors have become an increasingly prominent material for a wide range of active and passive devices from optoelectronics to high frequency and power electronics as well as photocatalysis. Regardless of the application, anisotropic etching is required for micro and nano structuring, currently performed by reactive ion etching (RIE). Alternately, metal-assisted chemical etching (MacEtch) is an open-circuit plasma-free anisotropic etching method that has demonstrated high aspect ratio device structures devoid of plasma-induced damage found in RIE. This paper presents an in-depth study of the ensemble electrochemical mechanisms that govern the photo-enhanced MacEtch process of GaN and related heterojunctions. Through in-depth experimental investigations, modeling and simulations, the effects of local cathode and anode design, energy-band alignments, and solution chemistry on MacEtch are correlated with the underlying electronic mechanisms of carrier generation, annihilation, transport, and extraction, establishing a fundamental framework for parametrized prediction of system behavior. These findings carry profound implications for tailored design of photoelectrochemical processes employed not just for uniformly etching wide/ultrawide bandgap materials but more broadly for semiconductor-based photocatalytic reactions in general. One-pot photo-enhanced MacEtching of AlInGaN multi-heterojunction device structures including superlattices and multi-quantum wells are demonstrated.

Published under an exclusive license by AIP Publishing. https://doi.org/10.1063/5.0186709

I. INTRODUCTION

GaN and other III-nitride semiconductors continue to push the boundaries for device performance in high power and frequency,[1–3] as well as optoelectronic[4–7] applications thanks to their wide bandgap, high electron mobility, proven heterojunctions, thermal stability, as well as strong resistance to radiation and chemical damage. The fabrication of these devices, especially with aggressively scaled dimensions, demand complex processes of which etching is a critical step. It is known that plasma-based dry etch, such as reactive ion etching causes crystal damage.[8] In some cases, the etching-induced damage is irreversible, while in other cases, it is too deep to be removed without substantial loss of materials and sidewall profiles.[9] Alternative etch methods are highly desirable.

Metal-assisted chemical etching (MacEtch) is an open circuit plasma-free anisotropic etching method.[10–12] It relies on a local catalysis-driven charge-transfer process to enable site-controlled etching with the distinct advantage of being free of ion-induced damage. Using MacEtch, superior etching properties and unparalleled damage-free device results have been demonstrated for a wide variety of semiconductors, such as Si,[13–15] Ge,[16] III-As,[17,18] III-P,[19,20] III-N,[21] SiC,[22] and Ga_2O_3[23,24] and related homo- and heterojunctions. For wide and ultra-wide bandgap semiconductors, because of the limited carrier mobilities, it is necessary to use above bandgap photons ($h\nu$) to generate free electron–hole (e^-–h^+) pairs and enhance MacEtch rate. The redox reaction in $h\nu$-MacEtch extracts the electrons from the

30 April 2024 15:54:17

Published under an exclusive license by AIP Publishing

semiconductor, drive charge imbalance with holes left at the surface to oxidize the semiconductor to generate porosity or etch away.[21–23,25,26] Over the past two decades, hν-MacEtch of III-nitrides have been studied as a function of etching chemistry[27,28] and semiconductor doping types.[29,30] However, the etch behavior control has mostly been *ad hoc*. The etching and structure design optimizations have not been accounted for holistically by considering the ensemble effects present during the etching process.

In this paper, we first investigate the effect of the geometric and material design of the metal electrodes by considering the size and distribution with respect to the semiconductor anode and by analyzing the effects of energy level alignment at the metal–semiconductor junction. We then study the effect of basic semiconductor properties, such as doping type, concentration, and resultant band energy level alignment between semiconductor and etchant junctions with implications for heterojunctions. Finally, we discuss the effects of solution composition, illumination, and other effects specific to the nitride etching system. By taking advantage of the combined electrochemical interactions in this study, we extend our discussion to the application of hν-MacEtch to 3D device structures consisting of device-relevant multi-heterojunction (multi-HJ) epitaxial stacks in both AlGaN and InGaN systems.

II. RESULTS AND DISCUSSION

Figure 1 illustrates the hν-MacEtch process of III-Nitrides, where the metal catalyst acts as a cathode for reduction reactions and the semiconductor plays the role of the anode for oxidation reactions. hν-MacEtch proceeds via photogeneration of free carriers in illuminated material as illustrated in Fig. 1(a). A metal catalyst (cathode) that is patterned on the semiconductor surface acts as a reduction mediator, transferring free electrons to an oxidant species present in the solution; in this case a persulfate ($S_2O_8^{2-}$) ion, which drives electron–hole pair separation as shown in Fig. 1(b) and is critical in preventing recombination. Continuous reduction of the oxidant species effectively acts as a charge sink with a potential bias allowing electron current to flow from the semiconductor to the cathode and then to the solution until the aqueous oxidant supply is exhausted. In addition to this, the metal patterns also block incoming light preventing photogeneration from occurring in the region immediately beneath the patterns. The local circuit is “completed” by the injection of remaining hole species to the nitride surface which oxidizes the material via bond reorganization.[31] The etchant within the solution proceeds to remove the III-N oxide as shown in Fig. 1(c). The combined act of surface oxidation and etching acts as the counter-process to the reduction-driven electron sink but for holes instead. The process repeats until it is terminated. Etch termination can occur via several pathways that are either chemical, electrical, or electrochemical in nature: quenching of the reaction, loss of illumination as well as etch stops that are chemically inert or electrically inactive. For simple reference of half reactions involving carriers, the reader is referred to Bardwell *et al.*[27] that provides a likely set of electrochemical equations with KOH as the

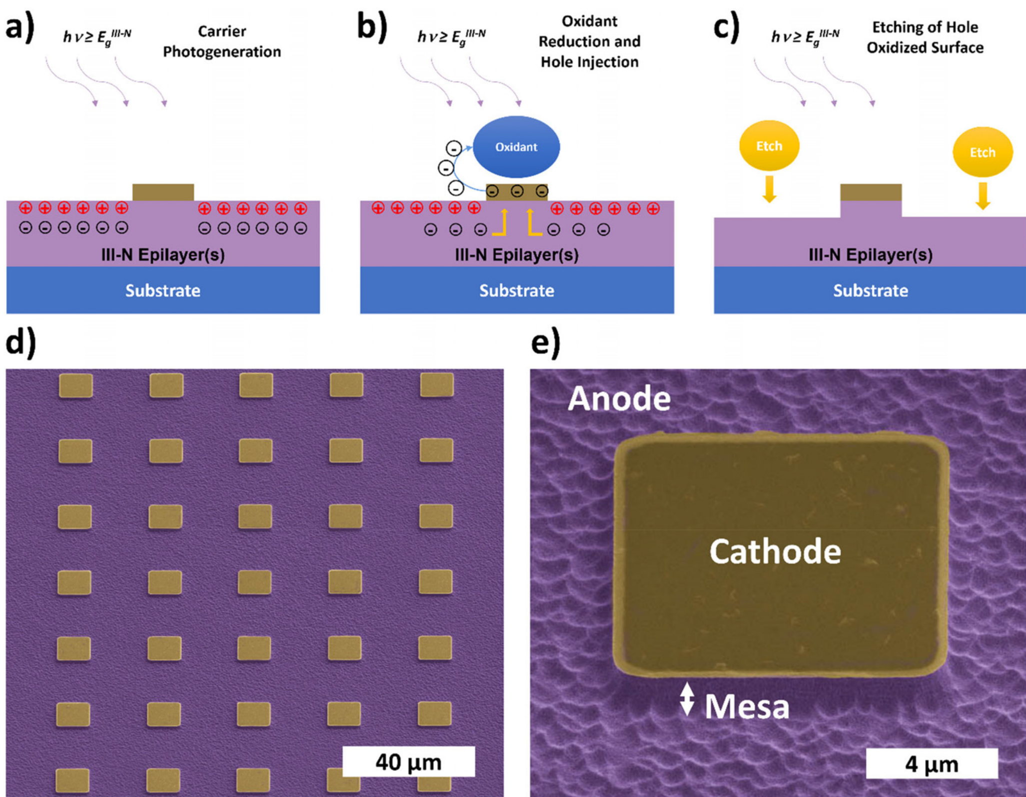

FIG. 1. Overview of the hν-MacEtch process: illustration (a–c) and false-color SEM images (d, e). (a) Carrier generation step (b) carrier separation via oxidant reduction reaction consuming electrons, (c) hole consumption via etching oxidized material completing localized circuit, (d) colorized SEM micrograph with metal pattern array, and (e) colorized SEM micrograph of single mesa structure formed by hν-MacEtch with electrodes labeled.

30 April 2024 15:54:17

Published under an exclusive license by AIP Publishing

etchant. It is noted that the exact stoichiometry is still unknown and is the subject of ongoing study.

hν-MacEtch ultimately consists of both a chemically driven component (derived from the etchant) and a photocurrent-driven component (derived from the catalyzed redox reaction) the latter of which is electronic in nature. Anisotropy and feature undercut are controlled by the balance between both components. Fundamentally, hν-MacEtch is a carrier-driven localized electrochemical redox process that is directly affected by the electronic properties of the materials involved and their interfaces (metal, semiconductor, and solution). It is noted that the hillock-like microscale roughness is derived from roughening by the KOH etchant consistent with well-known observations in the literature while nanoscale porosity is derived from oxidant decomposition. Both are specific to the etching solution used and can be mitigated with appropriate etchant selection evident in later discussion on solution chemistry.

A. Effects of cathode geometry and design

Though a variety of metals are often shown as catalysts in MacEtch, the geometric layout and energy alignment between the metal catalyst patterns and the target semiconductor are not well understood. We begin this section with discussion on the influence of both parameters on etch rate and implicitly on electron extraction and hole injection in n-type GaN.

It is well known that RIE possesses a loading effect, where the etch rate varies depending on the density and pattern of features on the wafer surface, as well as the aspect ratio (depth to width) of the etched features. High aspect ratio or densely packed features tend to have lower etch rates due to limited ion and radical access. However, it is crucial to note that loading can be influenced by several factors including the specific etching chemistry, process parameters (like power, pressure, and gas flow rates), and the design of the etching system. These factors in turn impact the distribution, availability of reactive species as well as the removal of etch byproducts and thus the extent of the loading effect.

Loading effects are also present in MacEtch processes,[14] but they manifest differently from RIE. In the forward MacEtch of Si, a distinct parabolic relationship between the vertical etch rate and the area to be etched has been observed. Initially, the etch rate rises with increasing feature size of the metal catalyst. However, as the catalyst size continues to increase, the etch rate begins to decrease. This dynamic is a result of the local competition between oxidant reduction catalyzed by the metal (which increases with cathode size), and mass transport occurring underneath the metal (which scales inversely with cathode size). The position and width of the parabolic peak can vary based on several factors including the etch conditions, semiconductor properties, type of metal catalyst, its morphology, pattern density, etc.

In the case of hν-MacEtch of GaN and other wide bandgap semiconductors, etching first occurs in areas that are exposed to external photons (i.e., regions not covered by the metal catalyst), adopting an "inverted" etch characteristic as seen in other materials such as InP, SiC, and ß-Ga_2O_3.[22,32,33] Therefore, within the constraints of carrier separation, hole injection occurs across the entire surface of the exposed semiconductor. Consequently, individual metal features collectively function in ensemble as a "global" cathode, counteracting the "global" semiconductor anode. Hence, up to a certain length scale, features of various dimensions would yield similar etch depths despite their presence patterned on the same substrate adjacent to one another. This represents a crucial distinction from the forward MacEtch scenario, with an example of this effect in GaN shown in supplementary material Fig. S1.

To study the effects of global cathode design on etching, we define several key parameters, namely,: the catalyst feature size, cathode–anode (C:A) ratio, and pattern coverage. For all results presented below, the etching conditions are identical utilizing a 1:12 molar concentration ratio of HCl:$K_2S_2O_8$ at room temperature for 10 mins, under the illumination of a UV lamp. Details of the experimental conditions can be found Sec. IV.

1. Effect of cathode:anode (C:A) ratio

From an electronic circuit viewpoint, the electrochemical system for hν-MacEtch behaves much like a two-terminal device. The patterned metal is the cathode with oxidant reduction mediated by the catalyst drawing electrons and the exposed semiconductor is the photoanode which provides both free carriers upon illumination. Surface oxidation and etching of the semiconductor simultaneously draws holes completing the circuit. When the total metal catalyst area is altered, it changes the proportion of the cathode to anode area, defined here as the C:A ratio.

To study the effect of geometry, we first vary the spacing between catalyst features. Figure 2(a) shows three structures produced by MacEtch. In these structures, the square array of catalyst patterns maintains a constant feature size of 10 μm, while the spacing varies from 18, 10, and 5 μm, resulting in corresponding C:A ratios of 10%, 20%, and 45% from left to right, respectively.

As the C:A ratio is increased from 1% to 45% as shown in Fig. 2(b), we find that the etch rate is maximized at around 10% and slowly tapers off as the C:A ratio approaches 45%. When the etch rate is converted to a volumetric scale (right Y axis), i.e., the total amount of material removed, the observed trend as a function of C:A ratio both in rising and falling edges are amplified. While the etch rate reduced only by less than 10% (from 55 to 50 nm/min) from C:A ratios of 10% to 45%, the volumetric removal rate dropped by 50% (from 21 000 to 14 000 μm^3/s). The volumetric scale is more representative of the overall electrochemical reaction as compared to traditionally reported etch rates, as can be seen from Fig. 2(a) where the increased feature packing density (from left to right) clearly shows that the actual volume removed is smaller. Under the etch condition specified, the inflection point for material removal rate is at just below a C:A ratio of 10%. The etch rate behavior observed is a result of the competition between the rate of hole injection, which increases with cathode area and the photogeneration of electrons and holes, which is proportional to the anode area. The C:A ratio is thus a reflection of photoelectrochemical (PEC) conversion with the peak position reflecting the maximum PEC system efficiency. As such, the C:A ratio is a coupled function of chemical reaction efficiency (oxidation, reduction, corrosion and mass transport) as well as photoelectronic conversion efficiency (carrier generation, transport and extraction).

It is important to note that, when compared to forward MacEtch (semiconductor beneath catalyst is etched), where the etch rate exhibits a parabolic relationship with feature size or spacing, the dynamics at play differ. In forward MacEtch, the factors in competition include hole injection and mass transport. However, in hν-MacEtch, which is fundamentally an inverse MacEtch process (semiconductor beneath

30 April 2024 15:54:17

Published under an exclusive license by AIP Publishing

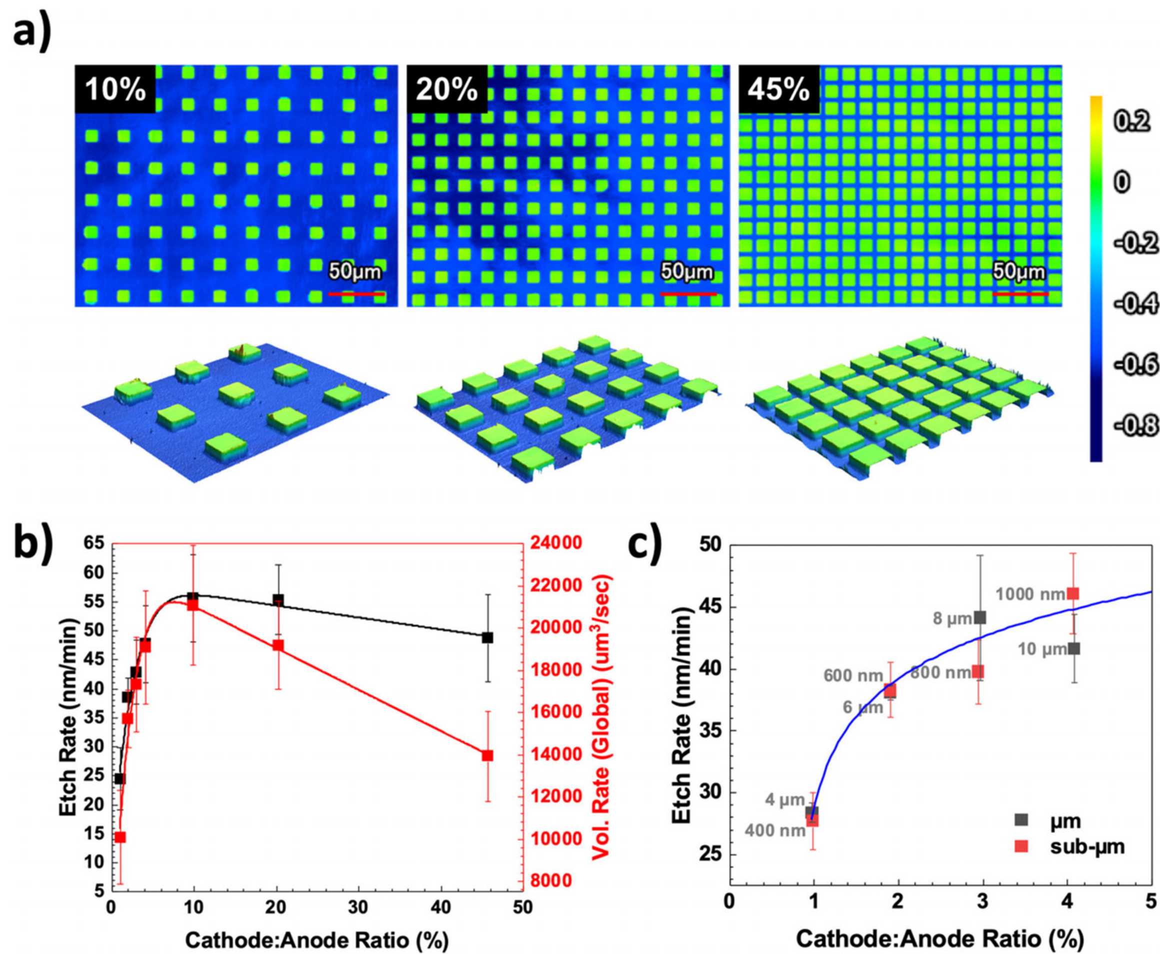

FIG. 2. Effect of cathode:anode (C:A) ratio. (a) Optical profile images (top and side-views) of GaN structures with varied C:A ratios. The metal catalyst feature size is 10 μm for all, while the spacings are 18, 10, and 5 μm, corresponding to for 10%, 20%, 45%, respectively, as indicated in the upper left corner; (b) etch and volumetric removal rate as a function of C:A ratio (constant feature size of 10 μm); and (c) etch rate of micrometer vs sub-micron features as a function C:A ratio. Note the Z-height in the 3D profiles are exaggerated by 700% for visual clarity. The color scale bar unit is μm.

catalyst is not etched), mass transport is not the limiting factor. Instead, the rate of hole injection (or electron extraction) competes with the carrier generation rate induced by external light, which is directly proportional to the exposed semiconductor area. These distinctions highlight the mechanisms at play in the hν-MacEtch process.

Additionally, we also study the effect of the C:A ratio at different feature dimensions. Figure 2(c) plots the etch rate as a function of C:A ratio in the range of 1%–4%, with both micrometer and sub-micrometer catalyst features (precise feature sizes labeled next to the data points). Over this range, the etch rate is enhanced with increasing C:A ratio, consistent with an electron extraction rate limited regime where an increase in cathode size allows for higher electron extraction and hole injection, leading to higher etch rate as observed previously in Fig. 2(b). Remarkably, the etch rate increase is similar for the same C:A ratio irrespective of the catalyst size, e.g., both 4 μm and 400 nm feature sizes yield about the same etch rate. The isolated effect of feature sizes with constant C:A ratio will be discussed later (Sec. II A 3).

2. Effect of cathode pattern distribution/coverage

When considering the geometrical design of the cathode, it is important to consider the effects of both the feature size and spacing of individual elements. To study the effect of feature spacing, we fix the total chip size ($5 \times 5\,\text{mm}^2$) while varying the pattern in the center of the chip. The number of elements in the pattern (27×27 square array) and element dimension ($9.6 \times 9.6\ \mu\text{m}^2$ squares) are kept constant, along with the metal catalyst composition and thicknesses (7 nm of Ta followed by 20 nm of Ru). The metal catalyst pattern coverage is defined as the ratio between the extent of the pattern field vs the chip edge length. The feature spacing and the corresponding pattern coverage (approximate) studied are listed in Table I along with pattern and chip diameters. For all four cases, the chip edge length is 5 mm (5000 μm) and the C:A ratio is 0.27%. The resulting etch optical profiles and representative line scans are shown in Fig. 3(a). Since the feature size is fixed, as the feature spacing increases, i.e., the elements are

30 April 2024 15:54:17

Published under an exclusive license by AIP Publishing

TABLE I. Effect of cathode pattern feature spacing and distribution/coverage on the etch rate.

Feature spacing (μm)	Pattern field (μm)	Chip edge length (μm)	Pattern coverage (%)	C:A ratio (%)	Etch rate (nm/min)
4.8	384	5000	8	0.27	12.6
12	571.2		12		13.1
29	1032		21		20.9
109	3105.6		62		24.8

more spread out and the total pattern area is increased, the corresponding pattern coverage is increased. Note that only the patterned area is shown here, while the outside of the pattern (27 × 27 square array) is exposed GaN with no metal coverage (this extends to the edge of the chip). As the spacing between cathodic elements increases (pattern coverage increases from 8% to 62% as labeled), the etch depth also increases.

Figure 3(b) shows the spatial distribution of the electron current density of the corresponding patterns with varied pattern coverage in Fig. 3(a), obtained using TCAD simulations, aiming to provide insights into the electronic behavior in MacEtch. Note that Figs. 3(c) and 3(d) show the same results for varied feature sizes and will be discussed shortly. Details of the modeling methodology and boundary condition can be found in the supplementary material. Figure 3(e) plots both the etch rate (left Y axis) and the simulated hole concentration (right Y axis) as a function of the pattern coverage. It can be seen that the simulated hole density follows a similar distribution trend to the etch rate, confirming that the studied hν-MacEtch conditions are largely electronically driven. The electronic origin of this trend is highlighted by simulations of the electron current density (j_e) in studied samples with two key observations. The first is that j_e is significantly higher at the edge of metal patterns (square pads), indicating that while oxidant reduction may occur across the entire metal surface, electron extraction is dominant at the edges. The second is that a finite j_e extends beyond the metal elements (into the background semiconductor) with a characteristic extraction length likely stemming from carrier mobility as shown in Fig. 3(b). The consequence of this is that as feature spacing approaches this characteristic length, the background j_e in the semiconductor is increased. As a result, there is a higher likelihood for generated holes to recombine with the extraction limited electrons in the background, reducing surface hole injection and is reflected by the reduction in etch rate. It is expected that there will be a limit to etch rate enhancement as cathodic element spacing increases, as is the case for C:A ratio, and the inflection point is associated with the regime limited by carrier transport.

3. Effect of cathode feature size

Recall that the etch rate converges to similar levels for both micrometer and sub-micrometer feature sizes for C:A ratios from 1% to 4% [Fig. 2(c)]. To effectively isolate the effects of feature size, we now scale the C:A ratio aggressively such that the total metal area (and consequently of the length from edges defined by patterns, i.e., the total circumference of all features combined) is increased as the element size is reduced. The feature dimensions, pattern array sizes and resulting scaling factor for the total metal area and edge length is summarized in Table II with the 9.6 μm feature size (highlighted) being the reference for scaling. Figure 3(d) shows the etch profiles and corresponding line scans for feature sizes of 2.4, 4.8, 7.2, and 9.6 μm as labeled, at a fixed feature spacing of 4.8 μm. The corresponding TCAD simulations [Fig. 3(d)] indicate that j_e is dominant at the edges of metal patterns irrespective of feature size, similar to that in Fig. 3(b). Note that chemically, the metal surface area for oxidant reduction is increased, and electronically, the extraction cross section for electrons is increased by the increase in edge length. As expected, when the extraction cross section is increased the etch rate also increases, which is a reflection of enhanced carrier separation between electrons and holes. Additionally, it is found that the magnitude is higher with smaller features likely due to the C:A ratio scaling as described previously and corresponds to the enhanced etch rate observed experimentally.

The etch rate and simulated hole density are plotted in Fig. 3(f) along with the scaling factors for both the total cathodic edge length and area as compared to the 9.6 μm feature size reference. When the etch rate for various features are normalized to a constant edge length by dividing the etch rate with the edge length or area scaling factor, we find that the normalized etch rate decreases as feature size reduces as shown in Fig. 3(g). This is indicative of two effects within the system. As the total surface area is normalized, we find that reducing the individual element dimension appears to reduce the carrier separation (implied by the etch rate reduction) even though there is an increase in extraction cross section (from increased edge length) suggesting a size-dependence with the oxidant reduction reaction. Furthermore, when the total extraction cross section is normalized, the etch rate reduction becomes even more dramatic suggesting in addition to the chemical side, there is also a size-dependent restriction on the electronic side where current extraction at individual elements may be constricted either by the electrode dimension, the presence of carrier trapping defects approaching the dimension of the electrode. This is evident in Fig. 1(c), where the sub-micrometer feature sizes show similar etch rate as the 10× larger micrometer size. We believe it is likely stemming from the presence of threading dislocations which appear as whisker-like features in etched regions of nitride material which is consistent with prior etching studies of this nature.[34–36] Typically, these possess a diameter of anywhere between 50 and 100 nm, suggesting that the influence of defects on carrier trapping (that prevents etching) is enhanced as sub-micrometer catalyst dimensions (i.e., 400 nm diameter squares) approach this trapping radius. Two key observations can be drawn from our simulations. First, the etch rate is a directly correlated with hole injection and second, the combined feature size and distribution effects dictate carrier utilization efficiency somewhat akin to electrical contact optimizations for photo-absorbing devices; both of which are electronic in nature with the C:A ratio as the overarching metric for combined PEC conversion efficiency.

We note that when patterns of varying dimensions are distributed across the sample in a quasi-randomized fashion, significant etch non-uniformities are not observed likely due to averaging of the above effects. As an example, Fig. S1 in the supplementary material shows a 3 × 3 mm^2 pattern field of randomly scaled patterns (in the form of text) and etch variation between three identical feature size sets in two randomly selected regions is found to be approximately 0.5 nm/min.

30 April 2024 15:54:17

Published under an exclusive license by AIP Publishing

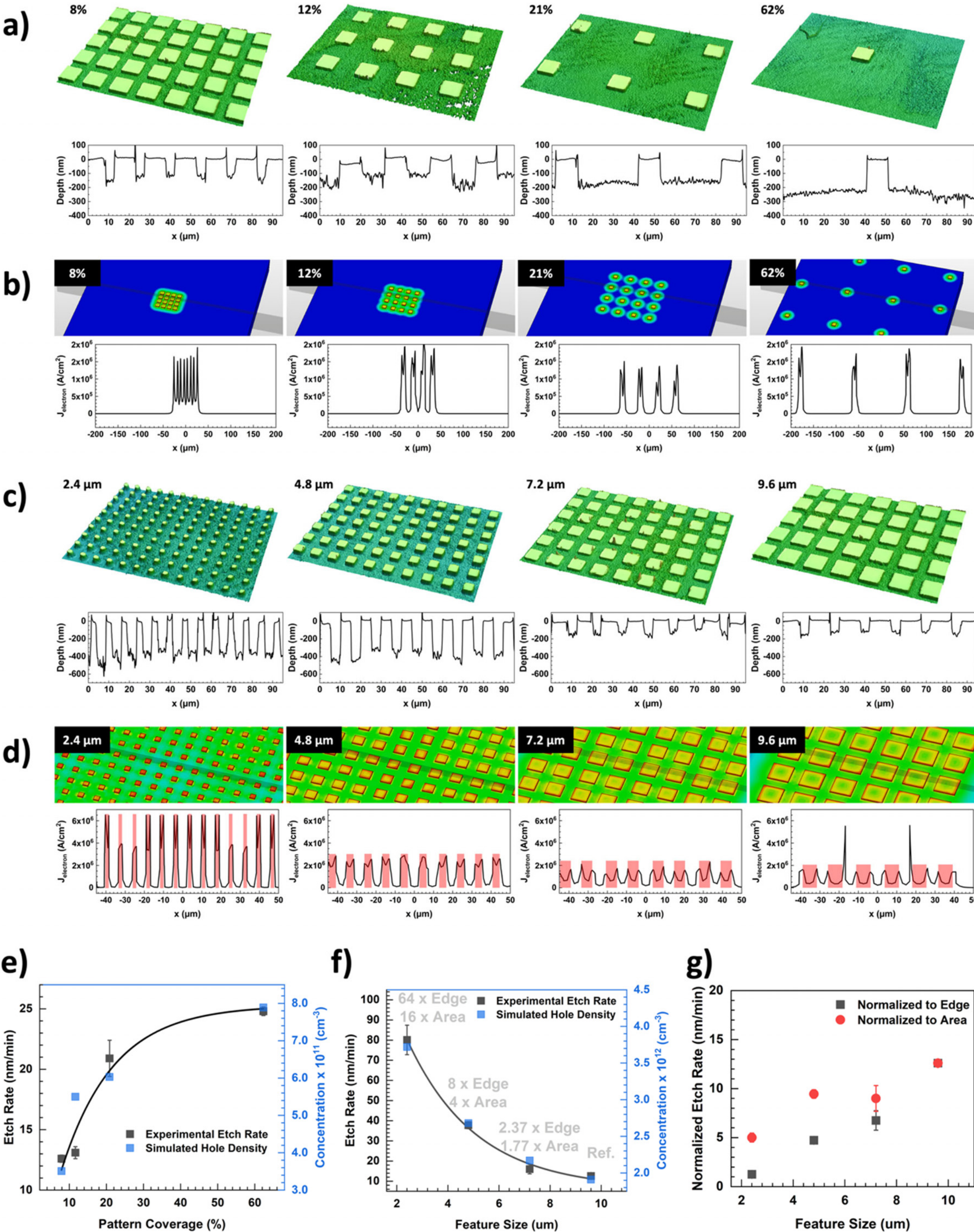

FIG. 3. MacEtch rate of n-GaN vs metal catalyst cathode feature size and distribution in a square array. [(a) and (c)] Optical profilometry scans and corresponding line scans for varied pattern coverage (8%, 12%, 21%, and 62%) and feature size (2.4, 4.8, 7.2, and 9.6 μm), respectively. [(b) and (d)] TCAD simulations of electron areal current density for the corresponding structures in (a) and (c), respectively. [(e) and (f)] Experimental etch rate and simulated hole density at the etch front plotted as a function of pattern coverage and feature size, respectively. (g) Area and edge normalized etch rate vs feature size. Catalyst and chip areas are constant. Si doping concentration of the n-GaN chip is 1×10^{18} cm^{-3}.

30 April 2024 15:54:17

Published under an exclusive license by AIP Publishing

TABLE II. Effect of cathode feature size and the corresponding scaling factors for metal area and edge length on the etch rate.

Feature size (μm)	Array size	Area scaling factor	Edge length scaling factor	C:A ratio (%)	Etch rate (nm/min)
2.4	432 × 432	16×	64×	4.30	80.1
4.8	108 × 108	2×	4×	1.07	37.8
7.2	48 × 48	1.33×	2.77×	0.48	16
9.6	27 × 27	1× (reference)	1x (reference)	0.27	12.6

4. *Effect of metal work function*

Electronic effects on etching extend beyond the geometric design of the cathode to the material composition of the electrodes themselves. When metals are deposited on the semiconductor surface, a Schottky barrier is formed with the barrier height dictated by the work function of the metal. Electronically, it is expected that the degree of band bending from energy level alignment will dictate the degree of electron flow toward the metal electrode barring any tunneling effects. To study the influence of work function, we must first distinguish between catalytic metals (i.e., Au and Pt group metals) and non-catalytic metals.

Here, the metal patterns are intentionally engineered such that they comprise of a catalytic metal capping layer (Ru) and a charge transfer layer (CTL) based on a lower work function metal such as Ta, Cr, and Ni (non-catalytic in this system). The associated energy alignments of the metal work function[37] as well as GaN conduction and valence band edges[38] are shown in Fig. 4(a). It is clear that all metals studied have energy alignments close to or below the mid-gap level of GaN and will cause varying degrees of upward band-bending. As the work function of the CTL (metal interlayer in direct contact with GaN) reduces from just over 5 eV to around 4.2 eV, the etch rate tends to rise (by approximately 40% in the studied range) as shown by Fig. 4(b) with an exponential dependence. From a diode operation perspective, the applied bias as well as potential barrier caused by the Schottky contact both possess an exponential dependence with current, which potentially contributes to the trend in experimental etch rate. From an electronic standpoint this corresponds to the hole injection at the semiconductor surface vs electron extraction which is what occurs at the CTL. It should be noted that the transfer of electrons from the catalyst surface to the solution is a separate affair and presents another condition that is dependent on both the chemical reactivity as well as catalytic strength of the metal.

B. Effects of semiconductor doping and band alignment

In this section, we focus on the effects of semiconductor properties pertaining to photocurrent generation and extraction at the anode. Previous studies have indicated that both hν-MacEtch[21] as well as PEC etching[29] possess similar doping dependencies, whereby etching was possible in n-type GaN but not p-type GaN when the catalyst is in direct contact with the semiconductor in question. This observation will be discussed and explained later in this section.

Our prior work has shown that as the doping concentration increases for n-type GaN, the etch rate was shown to increase and the chemical roughening from the active etchant was also shown to be reduced.[21] Mechanistically this is equivalent to biasing hν-MacEtch toward a photocurrent-driven etching process where the influence of the etchant is restricted to removal of hole-oxidized GaN. This is further supported with the fact that as doping concentrations increase the photogenerated current likewise increases. Under the assumption that carrier separation and hole transport is not the rate limiting factor, an increased hole generation rate would also lend to increased carrier injection at the semiconductor surface. In the case where mass transport limitations are not present in the solution (adsorption of etching

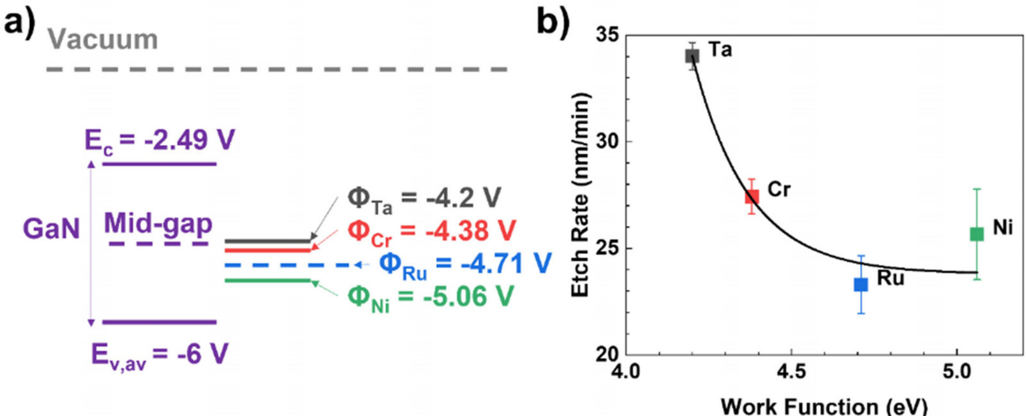

FIG. 4. Effect of metal work function. (a) Metal work function alignments to GaN conduction, valence band edges and mid-gap level with reference to vacuum and (b) etch rate trend against metal work function.

Published under an exclusive license by AIP Publishing

30 April 2024 15:54:17

species and desorption of product species) the etch rate increase observed is consistent with a photocurrent-driven process.

From the perspective of energy levels however, the doping concentration simply controls the fermi-level position, shifting this toward the conduction or valence band respectively. This in turn determines any potential band bending that may occur when the semiconductor is placed in contact with any other materials such as a metal as discussed in Sec. II A 4. Etching dependencies on doping type can also be effectively explained conceptually by potential band bending.

During the hν-MacEtch process, it is hypothesized that a virtual energy level (near mid-gap) exists for hole injection to occur (akin to redox reactions) from the semiconductor to semiconductor-liquid junction where the surface oxide is formed resulting in opposing band bending dependent on doping type when aligned with the fermi-level as shown in Fig. 5(a). With upward band bending in n-type materials, hole transport near the surface is directed toward the surface by the built-in potential while electrons are directed away, promoting overall surface hole injection. Conversely, with downward band bending in p-type materials, hole transport is directed toward the bulk of the material while electrons are driven toward the surface, slowing or quenching surface hole injection. In addition to this, the degree of band bending indicated by this hypothesis would also suggest that lighter doped n-type material will yield a weaker driving force (from a smaller built-in field) for holes resulting in a slower oxidation and etching, which is consistent with observed results previously cited. A similar conclusion can be drawn by examining the effects of individual dopant atoms on the positioning of the valence band maximum required for effective surface hole injection.

Using a DFT-based analysis model including surface coverage with explicitly dissociated water to approximate the solution environment, the effect of doping on the spatial distribution of the valence band maximum was investigated. For this purpose, a single Ga site was substituted with either a Mg (orange sphere) or Si (blue sphere) atom representing an extrema case of heavy n- or p-type doping, respectively, as shown in Figs. 5(b) and 5(c). The simulated surfaces depicted are m-plane as opposed to c-plane which is encountered experimentally to clearly isolate the effect of dopants by removing effects of polarization. Previous studies have shown that the intrinsic c-plane significantly decreases the bandgap and displays empty states in the valence band,[39] or occupied states in the conduction band when

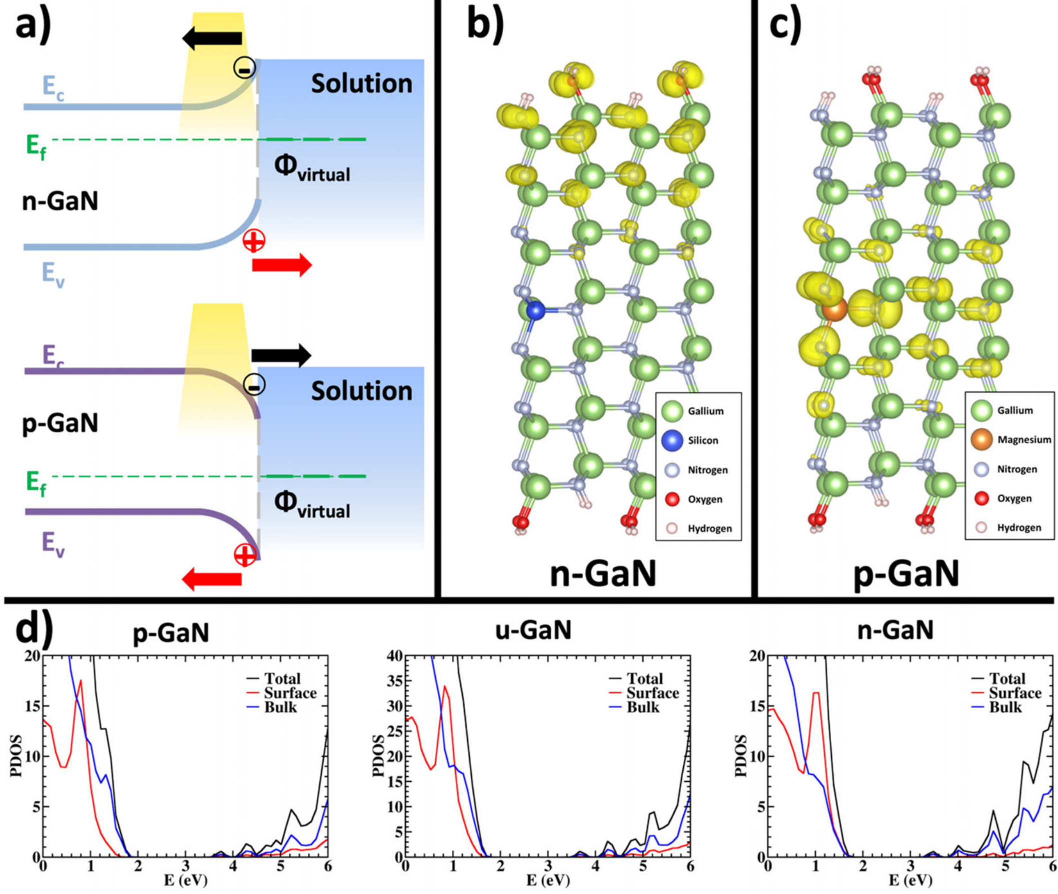

FIG. 5. Effect of doping. (a) hypothesized band bending of n and p-GaN vs solution, (b) simulated positions of valence band maximum in Si (blue atom) doped GaN, (c) simulated positions of valence band maximum in Mg (orange atom) doped GaN, and (d) DOS spatial contributions vs doping type around the GaN bandgap (full DOS provided in the supplementary material).

30 April 2024 15:54:17

Published under an exclusive license by AIP Publishing

adding hydrogens to saturate the dangling bonds.[40] This makes the interpretation of the effect of dopants on the c-plane challenging to disentangle from polarization effects, reconstruction and empty states in the valence band. We therefore use a model of the non-polar m-plane instead, to show the pushing/pulling effect the dopants employ, which result in different band bending behavior. It is found that the valence band maximum (represented by yellow lobes) can shift significantly from a surface- to bulk-based state depending on the dopant.

In the case of Mg doped GaN, the spatial distribution of the valence band maximum is localized in the bulk in close proximity to the Mg dopant. In the case of the Si dopant, the same valence band maximum shifts toward the surface of GaN. The contributions from surface and bulk DOS states for the conduction and valence bands are shown in Fig. 5(d) and a clear shift in spatial contribution is observed. As the doping type transitions from p-type to n-type, the surface state contribution becomes increasingly dominant. This presents a pathway for surface oxidation and is also in line with the effects of upward bending in n-type material, while the dominant bulk state contribution in p-type material confines spatial access away from the surface preventing oxidation. This is similar in many respects to energy level pinning by surface states as proposed by Youtsey *et al.*[29] but indicates the origin of dopant type-dependent etching for hν-MacEtch is likely from the spatial positioning of the valence band maxima.

While the general doping type dependency is the case for thick films of material, it is likely that it will play a smaller role when referencing thin films (such as quantum wells and quantum barriers) where chemical etching can greatly influence the etch-ability over a short length scale. While this phenomenon can appear problematic, it presents a unique opportunity to engineer built-in etch stops (via a suitable chemical system) to multi-HJ structures simply with the native nitride system.

On the other hand, while the doping type of individual layer can determine the etch-ability of the layer, it does not determine the etch-ability of composite structures since the described band alignment occurs at the etch-front only. Hence, carrier transport still occurs through a p-type or unintentionally doped material toward the metal catalyst and etching proceeds. This is conditional that the carrier extraction at the etch-front allows for hole-injection derived oxidation. We anticipate that similar band alignment with a virtual energy level will apply to the etch-ability of other III-N and wide bandgap materials like SiC and ß-Ga_2O_3 that rely on the hν-MacEtch process.

C. Solution and miscellaneous effects

When considering chemical effects, the solution is balanced between etchant and oxidant, which are the primary drivers of chemical and photocurrent-driven etching components of hν-MacEtch, respectively. Previously, we have established that an increase in oxidant-etchant ratio causes an increase in the etch rate, until the solution is rate-limited by active etchant concentration.[21] Much like the effect of increased dopant concentration, an increase in oxidant concentration drives hν-MacEtch toward a predominantly photocurrent-driven process. Unlike the case of dopant concentration which affects the supported current density in the semiconductor material, the oxidant concentration affects the extracted current density at the metal, acting as a potential bias on the cathode as the electronic parallel.

1. Acid vs base MacEtch chemistries

While the electronic effects discussed are translatable between differing material systems and structures, the chemical effects more specific to etching the III-N material system are not and must be addressed. The most widely studied choice of etchant and oxidant is KOH and $K_2S_2O_8$ respectively since the conception of electrochemical etching in GaN.[27–29] Though the KOH system is effective for etching Ga and Al containing nitrides, its basic pH presents a challenge when etching In containing nitrides. The chemical origin for this stems from the pH-dependent solubility of the group III metal oxides and hydroxides. While Ga and Al derivatives are largely amphoteric in nature, In derivatives tend to be less soluble in basic media.[41]

To enable one-pot etching for AlInGaN (the most widely employed nitride system), we have developed a previously unreported combination of HCl (etchant) with the same $K_2S_2O_8$ (oxidant) as the sole components of the hν-MacEtch solution. The impetus for this combination, beyond the clear need for acidic media is multi-fold. The first is to maintain the original bi-component nature of etchant and oxidant found ubiquitously in MacEtch irrespective of material. The second is to maintain a singular pH environment despite temporal decomposition of the oxidant.[28] Finally, the third is to introduce a chemistry that can potentially produce lower boiling point reaction products as opposed to gallate (found with hydroxides) or fluoride (found with HF) salts, providing a potential pathway toward scaling etching beyond solution to vapor phase on the etchant side. While we have successfully employed this combination of etchants in this study, there are a few concessions that must be made when utilizing HCl as the active etchant. The first is the corrosive nature of HCl proves to be a challenge to finding the appropriate combination of metals that are not corroded significantly to provide reliable and consistent etching. One such combination described is via a Ru catalyst and Ta CTL, though it is known that Pt can also act in the same capacity as a catalytic layer. The second is that the pH stability provided by the acid chemistry simply masks the inherent problem with utilizing a persulfate oxidant which inevitably decomposes with an acidic by-product, though this is still more photo-stable than more traditional MacEtch oxidants, such as hydrogen peroxide.

2. Effect of solution concentration

One key aspect of the solution apart from molar ratios discussed previously is the concentration or dilution of the entire etchant itself. Initial studies performed at a 1:12 HCl:$K_2S_2O_8$ molar ratio with a fixed feature size (10 μm), substrate dimension ($5 \times 5\,mm^2$) and C:A ratio ($\sim$10%) showed an inverse relation between dilution and etch rate as expected in a chemical etch but with a non-linear behavior whereby a 10$\times$ dilution (100% to 10% relative concentration) of the hν-MacEtch solution yields a reduction of around 50% in etch rate (nearly 90 to 40 nm/min) as shown in Fig. S2, which can allow reduction of chemical corrosion while reducing impact on anisotropic etching.

3. Effect of solution chemistry on sample morphology

Briefly, in the case of both KOH and HCl etchants, undercut is observed to be present but appears to be inconsistent with solution concentrations with the same etchant to oxidant ratio. This points to sources such as reactive chemical species (from water or the etchant)

30 April 2024 15:54:17

Published under an exclusive license by AIP Publishing

formed by the high energy UV light source and not the decomposed oxidant. Morphologically, it is notable that unlike the known crystal faceting and pyramid-like roughening in KOH chemistry, HCl yields a uniform, quasi-porous surface which we attribute to corrosion from byproducts of persulfate thermal and photodecomposition. It should be noted that prior to oxidant decomposition the morphology is governed by the balance between the HCl as well as basic species derived from the cation present in the oxidant (in this case, K^+). This is evident from the fact that without the pH stabilization, the KOH chemistry yields a similar morphology to the HCl etch system. On the other hand, when HCl concentration is increased the porosity is reduced. Finally on a macroscopic scale, the HCl chemistry is observed to achieve mm scale uniformity across the pattern surface while this is achieved in the KOH chemistry only under heated conditions (in this case, 85 °C), suggesting mass transport differences between the two etchants that require consideration both from a uniformity perspective as well as PEC efficiency perspective as described previously. SEM micrographs and optical profilometry scans detailing feature undercut (Fig. S3) as well as etch uniformity (Fig. S4) under heated and unheated conditions are available in the supplementary material.

4. *Effect of illumination source*

Finally, while the core of this study has largely comprised electrochemical effects, the effects of photon energy and intensity are significant and should also be noted. There are a few obvious parameters that are affected by photon energy or intensity. These include the carrier generation rate (controlling current available for extraction), the energy for carriers to surpass potential barriers in the case of multi-nitride structures, as well as wavelength-dependent photodecomposition rate of reactants in the hν-MacEtch solution. The complexity for analysis is increased when we consider that the light source used in this experiment has a wide emission spectrum and the precise wavelengths that either enable or cause the above is not clear (a range however can be surmised). A monochromatic light source with sufficient illumination area would likely need to be employed in conjunction with the environmental controls in this study and can be a subject of investigation by itself.

D. Correlating PEC system with electronic effects in GaN

A summary of key controlling parameters in hν-MacEtch by PEC category that can be modeled and translated to other PEC systems are summarized in Table III with associated electronic terms as discussed in this study.

The component analysis performed in this study for the hν-MacEtch process suggests that etching as well as PEC systems in general, can be electronically modeled in a similar fashion to devices, providing a powerful prediction pathway for process adjustment geared toward in multi-HJ device applications.

E. Etching in device-relevant Multi-HJ epitaxial structures

As part of this study, we show that with careful considerations of the ensemble effects discussed previously, it is possible to effectively etch multi-HJ structures in a similar fashion to bulk materials. This is first demonstrated with a superlattice structure consisting of seven pairs of 15 nm $Al_{0.16}Ga_{0.84}N$/95 nm GaN prepared by metal organic chemical deposition (MOCVD) atop of a GaN template. The structure is doped n-type with Si $\sim 3 \times 10^{18}$ cm^{-3}. As can be seen in Fig. 6(a), micropillar arrays consisting of a superlattice stack atop the substrate template is produced via the discussed HCl chemistry. The corresponding layer structure is depicted in Fig. 6(b). While the morphology between the superlattice stack and substrate is pronounced (primarily from differences in growth), the AlGaN and GaN layers cannot be easily distinguished within the epilayer stack itself appearing to be homogenous as shown in Fig. 6(c). The primary considerations in this case consist of both the light source, which must satisfy energetically both bandgaps present in the composite structure as well as solution concentration optimization, the latter of which takes advantage of hν-MacEtch and chemical etch rate non-linearity to overcome the increase in chemical selectivity between GaN and AlGaN as a result of Al composition,[42] which would otherwise show recessed AlGaN layers as a result of pure chemical corrosion; a stain etch revealing this can be found in Fig. 6(d).

In addition to this, we also show for the first time that commercially grown LED epi-layers composed of AlInGaN materials can also be etched via the newly developed HCl chemistry with the p-side first etched via RIE. The layer structure as well as colorized SEM image depicting the mesa sidewall is shown in Fig. 6(e) with distinct interfaces between the purple p (~90 nm), turquoise and green InGaN multi-quantum well (MQW) active structure (~480 nm) as well as blue n layers (total > 2 μm, ~200 nm etched as shown). Etch optimization was not performed in this case but it is found that exposed p-type layers can in fact be entirely etched through when the catalyst isn't directly placed atop the layer, suggesting appropriate catalyst

TABLE III. Cross-correlation of etch system parameters and their electronic equivalent terms in three categories of PEC configurations: solution, cathode, and anode.

Etch system parameter	Electronic effect	PEC configuration category
Oxidant:etchant ratio	Applied potential bias (V_{app})	Solution composition
Feature size and radial distribution	Extraction cross section (A_{ext}) & Series resistance (R_s)	Cathode geometric and material design
Cathode:anode (C:A) ratio	Electrochemical efficiency (η)	
CTL work function	Electron potential barrier (ϕ_b^{e-})	
Doping concentration	Supported current density (J)	Anode semiconductor properties
Doping type	Hole potential barrier (ϕ_b^{h+})	

30 April 2024 15:54:17

Published under an exclusive license by AIP Publishing

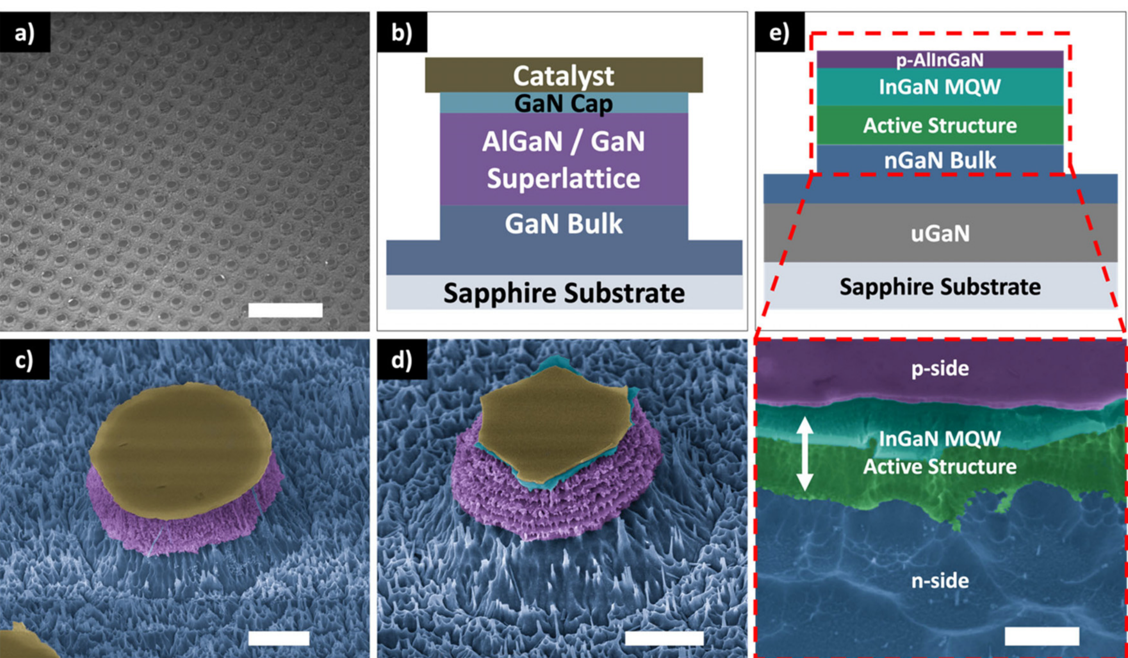

FIG. 6. MacEtch of III-N heterojunctions. (a) Overview of AlGaN/GaN superlattice micropillar array, (b) color matched structure of micropillar, (c) colorized view of single pillar, (d) colorized view of single pillar after chemical recess etch, and (e) color matched structure of commercial blue InGaN/GaN LED epitaxial structure with colorized view of device mesa produced by MacEtch. Scale bars are 20 μm for (a), 1 μm for (c) and (d) and 500 nm for (e).

30 April 2024 15:54:17

placement can enable etching that is non-selective to doping type. In this instance, the catalyst was patterned atop of the MQW structure instead of the p-type capping layer. Electrons are thus drawn away from the p-type layer surface which would reduce carrier recombination at the etch front. This enables hole-injection which is the prerequisite for MacEtch to occur and is consistent with other studies[30] based around carrier separation as the primary driving force to enable p-type etching. As a side note, differences in etch morphology in both the AlGaN/GaN superlattice as well as InGaN MQW structures, are attributed to the combined effects of chemical corrosion and variations in III-N growth conditions. In relation to both superlattice and device structures, the charge separation dependence required for hν-MacEtch also suggests that carrier blocking layers in device structures (such as optoelectronic devices) can potentially interfere with etching of multi-HJs and should be accounted for to assure the appropriate carrier type can bypass the target layer.

III. CONCLUSIONS

With the ever-increasing prevalence of nitride materials from optoelectronic to RF and power applications comes process challenges as devices continue to scale for performance enhancements. Material damage induced by conventional RIE etching proves to be a major hurdle that is often increasingly detrimental to performance as devices scale. MacEtch has proven its viability in producing structures devoid of plasma damage with a similar throughput to RIE. In this study, we demonstrate that multi-HJs can effectively be etched homogeneously via a new, one-pot HCl chemistry across the widespread AlInGaN material system ranging from superlattice structures to device structures with Al and In fractions of up to approximately 16% in each case. More fundamentally, we reveal the governing mechanics to the electrochemical process that occurs during hν-MacEtch. We identify consequential effects on carrier extraction with cathode materials and geometric design, balance between the metal cathode and semiconductor anode areas as well as energy level alignments between dissimilar material interfaces with varying metal work function and semiconductor doping-dependent fermi-levels. By correlating the above design parameters with their electronic counterparts, we establish a basic framework that allows for translation beyond the AlInGaN system to not just emerging nitride materials such as AlScN but other wide bandgap semiconductors such as SiC and ß-Ga_2O_3, all of which have been shown or are expected to follow the hν-MacEtch process. Crucially, the electronic effects studied in this work enables system-specific modeling of carrier extraction. This can be on a device-by-device basis depending on both the multi-HJ structure and the geometric layout. It can also be for an application-specific basis such as photocatalysis depending on both electrode design and energy level alignments of redox processes. In summary, this study has moved the hν-MacEtch process beyond reported bulk materials to multi-HJ stacks involving materials across the AlInGaN system, demonstrating viability required for device-relevant processing of 3D nitride structures. While several manufacturing specific aspects such as reproducibility and process control require continued development, it is important to note that we have, for the first time, successfully cross-correlated process design parameters with baseline electronic effects. This significant advancement paves way for device and application specific modeling, providing a powerful prediction pathway for processing that extends beyond hν-MacEtch of nitride and wide bandgap

Published under an exclusive license by AIP Publishing

materials to encompass other PEC systems utilizing similar electronic materials.

While this study has established the baseline electronic framework for hν-MacEtch and similar PEC processes via the III-N materials system, there are additional parameters that remain to be explored. This includes the effects of illumination energy both on carrier generation and transport processes in multi-HJs and separately, its effects on solution temporal photostability. Closely inter-linked is the chemical redox system itself which governs both native corrosion as well as carrier-driven corrosion, the latter of which determines hole consumption rate and contributes to the overall efficiency of the electrochemical system.

IV. EXPERIMENTAL METHODS

GaN samples grown by MOCVD on single side polished sapphire substrates were purchased commercially from SinoVio Semiconductor. The GaN/AlGaN superlattice structure was grown using a close-coupled showerhead MOCVD reactor, with TMGa, TMAl, and SiH_4 for Ga, Al, and Si, sources, respectively. The GaN/InGaN blue LED epitaxial structure grown by MOCVD on double side polished sapphire samples was purchased commercially from Enkris Semiconductor.

Depending on feature sizes, metal catalyst patterns were produced with conventional photolithography using a Heidelberg MLA 150 direct laser (375 nm) writer or an Elionix ELS-G150 electron beam lithography system. Metals utilized in this study were deposited via a K.J. Lesker PVD 75 electron beam evaporation system or an AJA 4 Orion-8 magnetron sputtering system. Etching was performed in a solution of deionized (DI) water, hydrochloric acid (HCl) or potassium hydroxide (KOH) and potassium persulfate ($K_2S_2O_8$) with varying molar ratios of each component. A pH buffer of Na_3PO_4 was included with matching molar concentration to the oxidant for KOH-based etching. Sample illumination was provided by a Dymax BlueWave® 200 UV spot curing lamp. The illumination lamp, with a power density of $\sim$17 W/cm^2 across a 300–450 nm emission range, was affixed at approximately 5 cm away from the sample. The solution to air interface is adjusted to be approximately 2 mm above the sample surface during etching. Samples were characterized using a FEI SEM for morphology and a Keyence VK-X1000 3D laser scanning confocal microscope for depth profiles.

Modeling of carrier and current densities were performed via a TCAD simulation framework in Sentaurus using the finite element method with Newton iterations. Modeling of the valence band maximum spatial distribution was performed via the Vienna *Ab initio* Simulation Package with the PBE exchange correlation functional. Additional details for both simulation methodologies can be found in the supplementary material.

SUPPLEMENTARY MATERIAL

See the supplementary material for the discussion of etch uniformity of quasi-randomly sized features, effect of solution concentration, analysis of catalyst undercutting, etch uniformity of heated and un-heated solutions, and simulation methodology for TCAD and DFT results.

ACKNOWLEDGMENTS

This work was supported in part by United States Army Research Office (Award No. W911NF2110337) and National Science Foundation DMR (Award No. 2329107).

AUTHOR DECLARATIONS

Conflict of Interest

The authors have no conflicts to disclose.

Author Contributions

Clarence Y. Chan: Conceptualization (equal); Data curation (equal); Formal analysis (equal); Investigation (lead); Methodology (equal); Visualization (equal); Writing – original draft (equal); Writing – review & editing (equal). **Shaloo Rakheja:** Resources (equal); Supervision (equal); Writing – review & editing (supporting). **Victor S. Batista:** Funding acquisition (equal); Resources (equal); Supervision (equal); Writing – review & editing (supporting). **Zetian Mi:** Funding acquisition (equal); Resources (equal); Supervision (equal); Writing – review & editing (supporting). **Xiuling Li:** Conceptualization (equal); Funding acquisition (equal); Methodology (equal); Project administration (equal); Resources (equal); Supervision (equal); Writing – original draft (equal); Writing – review & editing (equal). **Jan Paul Menzel:** Data curation (supporting); Formal analysis (equal); Methodology (supporting); Software (equal); Visualization (supporting); Writing – review & editing (supporting). **Yicong Dong:** Data curation (supporting); Formal analysis (equal); Methodology (supporting); Software (equal); Visualization (supporting); Writing – review & editing (supporting). **Zhuoran Long:** Data curation (supporting); Formal analysis (equal); Methodology (supporting); Software (equal); Visualization (supporting); Writing – review & editing (supporting). **Aadil Waseem:** Writing – review & editing (supporting). **Xihang Wu:** Writing – review & editing (supporting). **Yixin Xiao:** Resources (equal); Writing – review & editing (supporting). **Jinqiao Xie:** Resources (equal); Writing – review & editing (supporting). **Edmond Chow:** Resources (equal); Writing – review & editing (supporting).

DATA AVAILABILITY

The data that support the findings of this study are available from the corresponding author upon reasonable request.

REFERENCES

[1] J. Y. Tsao, S. Chowdhury, M. A. Hollis, D. Jena, N. M. Johnson, K. A. Jones, R. J. Kaplar, S. Rajan, C. G. Van de Walle, E. Bellotti, C. L. Chua, R. Collazo, M. E. Coltrin, J. A. Cooper, K. R. Evans, S. Graham, T. A. Grotjohn, E. R. Heller, M. Higashiwaki, M. S. Islam, P. W. Juodawlkis, M. A. Khan, A. D. Koehler, J. H. Leach, U. K. Mishra, R. J. Nemanich, R. C. N. Pilawa-Podgurski, J. B. Shealy, Z. Sitar, M. J. Tadjer, A. F. Witulski, M. Wraback, and J. A. Simmons, "Ultrawide-bandgap semiconductors: Research opportunities and challenges," Adv. Electron. Mater. **4**(1), 1600501 (2018).

[2] J. P. Kozak, R. Zhang, M. Porter, Q. Song, J. Liu, B. Wang, R. Wang, W. Saito, and Y. Zhang, "Stability, reliability, and robustness of GaN power devices: A review," IEEE Trans. Power Electron. **38**(7), 8442–8471 (2023).

[3] H. Amano, Y. Baines, E. Beam, M. Borga, T. Bouchet, P. R. Chalker, M. Charles, K. J. Chen, N. Chowdhury, R. Chu, C. De Santi, M. M. De Souza, S. Decoutere, L. Di Cioccio, B. Eckardt, T. Egawa, P. Fay, J. J. Freedsman, L. Guido, O. Häberlen, G. Haynes, T. Heckel, D. Hemakumara, P. Houston, J. Hu, M. Hua, Q. Huang, A. Huang, S. Jiang, H. Kawai, D. Kinzer, M. Kuball, A. Kumar, K. B. Lee, X. Li, D. Marcon, M. März, R. McCarthy, G. Meneghesso, M. Meneghini, E. Morvan, A. Nakajima, E. M. S. Narayanan, S. Oliver, T. Palacios, D. Piedra, M. Plissonnier, R. Reddy, M. Sun, I. Thayne, A. Torres, N. Trivellin, V. Unni, M. J. Uren, M. Van Hove, D. J. Wallis, J. Wang, J. Xie, S. Yagi, S. Yang, C. Youtsey, R. Yu, E. Zanoni, S. Zeltner, and Y. Zhang, "The 2018 GaN power electronics roadmap," J Phys. D. Appl. Phys. **51**(16), 163001 (2018).

30 April 2024 15:54:17

Published under an exclusive license by AIP Publishing

[4]C. Xie, X. Lu, X. Tong, Z. Zhang, F. Liang, L. Liang, L. Luo, and Y. Wu, "Recent progress in solar-blind deep-ultraviolet photodetectors based on inorganic ultrawide bandgap semiconductors," Adv. Funct. Mater. **29**(9), 1806006 (2019).
[5]J. Ryu, S. Park, Y. Park, S. Ryu, K. Hwang, and H. W. Jang, "Technological breakthroughs in chip fabrication, transfer, and color conversion for high-performance micro-LED displays," Adv. Mater. **35**, e2204947 (2023).
[6]R. Gujrati, A. Srivastava, P. Vuong, V. Ottapilakkal, Y. N. Sama, T. H. Ngo, T. Moudakir, G. Patriarche, S. Gautier, P. L. Voss, S. Sundaram, J. P. Salvestrini, and A. Ougazzaden, "Multiple shapes micro-LEDs with defect free sidewalls and simple liftoff and transfer using selective area growth on hexagonal boron nitride template," Adv. Mater. Technol. **8**(15), 2300147 (2023).
[7]J. Y. Lin and H. X. Jiang, "Development of microLED," Appl. Phys. Lett. **116**(10), 100502 (2020).
[8]Q. Fan, S. Chevtchenko, X. Ni, S.-J. Cho, F. Yun, and H. Morkoç, "Reactive ion etch damage on GaN and its recovery," J. Vacuum Sci. Technol. B **24**(3), 1197 (2006).
[9]T. Kumabe, Y. Ando, H. Watanabe, M. Deki, A. Tanaka, S. Nitta, Y. Honda, and H. Amano, "Etching-induced damage in heavily Mg-doped p-type GaN and its suppression by low-bias-power inductively coupled plasma-reactive ion etching," Jpn J. Appl. Phys. **60**(SB), SBBD03 (2021).
[10]Z. Huang, N. Geyer, P. Werner, J. de Boor, and U. Gösele, "Metal-assisted chemical etching of silicon: A review," Adv. Mater. **23**(2), 285–308 (2011).
[11]X. Li, "Metal assisted chemical etching for high aspect ratio nanostructures: A review of characteristics and applications in photovoltaics," Curr. Opin. Solid State Mater. Sci. **16**(2), 71–81 (2012).
[12]X. Li and P. W. Bohn, "Metal-assisted chemical etching in HF/H_2O_2 produces porous silicon," Appl. Phys. Lett. **77**(16), 2572–2574 (2000).
[13]L. L. Janavicius, J. A. Michaels, C. Chan, D. J. Sievers, and X. Li, "Programmable vapor-phase metal-assisted chemical etching for versatile high-aspect ratio silicon nanomanufacturing," Appl. Phys. Rev. **10**(1), 011409 (2023).
[14]J. D. Kim, P. K. Mohseni, K. Balasundaram, S. Ranganathan, J. Pachamuthu, J. J. Coleman, and X. Li, "Scaling the aspect ratio of nanoscale closely packed silicon vias by MacEtch: Kinetics of carrier generation and mass transport," Adv. Funct. Mater. **27**(12), 1605614 (2017).
[15]J. C. Shin, D. Chanda, W. Chern, K. J. Yu, J. A. Rogers, and X. Li, "Experimental study of design parameters in periodic silicon micropillar array solar cells produced by soft lithography and metal assisted chemical etching," IEEE J. Photovoltaics **2**, 129 (2012).
[16]M. Kim, S. Yi, J. D. Kim, X. Yin, J. Li, J. Bong, D. Liu, S. C. Liu, A. Kvit, W. Zhou, X. Wang, Z. Yu, Z. Ma, and X. Li, "Enhanced performance of Ge photodiodes via monolithic antireflection texturing and α-Ge self-passivation by inverse metal-assisted chemical etching," ACS Nano **12**(7), 6748–6755 (2018).
[17]L. Kong, Y. Song, J. D. Kim, L. Yu, D. Wasserman, W. K. Chim, S. Y. Chiam, and X. Li, "Damage-free smooth-sidewall InGaAs nanopillar array by metal-assisted chemical etching," ACS Nano **11**(10), 10193–10205 (2017).
[18]P. K. Mohseni, S. H. Kim, X. Zhao, K. Balasundaram, J. D. Kim, L. Pan, J. A. Rogers, J. J. Coleman, and X. Li, "GaAs pillar array-based light emitting diode fabricated by metal-assisted chemical etching," J. Appl. Phys. **114**, 064909 (2013).
[19]Y. Song, P. K. Mohseni, S. H. Kim, J. C. Shin, T. Ishihara, I. Adesida, and X. Li, "Ultra-high aspect ratio InP junctionless FinFETs by a novel wet etching method," IEEE Electron Device Lett. **37**(8), 970–973 (2016).
[20]C. Y. Chan, H. C. Roberts, Y. Xiao, P. J. Froeter, D. J. Sievers, Z. Mi, and X. Li, "Plasma-damage free efficiency scaling of micro-lEDs by metal-assisted chemical etching," Adv. Opt. Mater. (published online).
[21]C. Y. Chan, S. Namiki, J. K. Hite, M. A. Mastro, S. B. Qadri, and X. Li, "Homoepitaxial GaN micropillar array by plasma-free photo-enhanced metal-assisted chemical etching," J. Vacuum Sci. Technol. A **39**(5), 053212 (2021).
[22]J. A. Michaels, L. Janavicius, X. Wu, C. Chan, H. Huang, S. Namiki, M. Kim, D. Sievers, and X. Li, "Producing silicon carbide micro and nanostructures by plasma-free metal-assisted chemical etching," Adv. Funct. Mater. **31**(32), 2103298 (2021).
[23]H.-C. Huang, Z. Ren, A. F. M. Anhar Uddin Bhuiyan, Z. Feng, Z. Yang, X. Luo, A. Q. Huang, A. Green, K. Chabak, H. Zhao, and X. Li, "β-Ga_2O_3 FinFETs with ultra-low hysteresis by plasma-free metal-assisted chemical etching," Appl Phys Lett **121**(5), 052102 (2022).
[24]Z. Ren, H. C. Huang, H. Lee, C. Chan, H. C. Roberts, X. Wu, A. Waseem, A. Bhuiyan, H. Zhao, W. Zhu, and X. Li, "Temperature dependent characteristics of β-Ga_2O_3 FinFETs by MacEtch," Appl Phys Lett **123**(4), 043505 (2023).
[25]H. C. Huang, M. Kim, X. Zhan, K. Chabak, J. D. Kim, A. Kvit, D. Liu, Z. Ma, J. M. Zuo, and X. Li, "High aspect ratio β-Ga_2O_3 fin arrays with low-interface charge density by inverse metal-assisted chemical etching," ACS Nano **13**(8), 8784–8792 (2019).
[26]M. Kim, H. C. Huang, J. D. Kim, K. D. Chabak, A. R. K. Kalapala, W. Zhou, and X. Li, "Nanoscale groove textured β-Ga_2O_3 by room temperature inverse metal-assisted chemical etching and photodiodes with enhanced responsivity," Appl. Phys. Lett. **113**(22), 222104 (2018).
[27]J. A. Bardwell, J. B. Webb, H. Tang, J. Fraser, and S. Moisa, "Ultraviolet photoenhanced wet etching of GaN in $K_2S_2O_8$ solution," J. Appl. Phys. **89**(7), 4142–4149 (2001).
[28]D. M. Dryden, R. J. Nikolic, and M. S. Islam, "Photogalvanic Etching of n-GaN for Three-Dimensional Electronics," J. Electron. Mater. **48**(5), 3345–3350 (2019).
[29]C. Youtsey, G. Bulman, and I. Adesida, "Dopant-selective photoenhanced wet etching of GaN," J. Electron. Mater. **27**(4), 282–287 (1998).
[30]A. C. Tamboli, A. Hirai, S. Nakamura, S. P. Denbaars, and E. L. Hu, "Photoelectrochemical etching of p-type GaN heterostructures," Appl. Phys. Lett. **94**(15), 151113 (2009).
[31]H. Gerischer, "Photodecomposition of semiconductors thermodynamics, kinetics and application to solar cells," Faraday Discuss. Chem. Soc. **70**, 137 (1980).
[32]S. H. Kim, P. K. Mohseni, Y. Song, T. Ishihara, and X. Li, "Inverse metal-assisted chemical etching produces smooth high aspect ratio InP nanostructures," Nano. Lett. **15**(1), 641–648 (2015).
[33]H.-C. Huang, Z. Ren, C. Chan, and X. Li, "Wet etch, dry etch, and MacEtch of β-Ga_2O_3: A review of characteristics and mechanism," J. Mater. Res. **36**(23), 4756–4770 (2021).
[34]J. A. Bardwell, I. G. Foulds, J. B. Webb, H. Tang, J. Fraser, S. Moisa, and S. J. Rolfe, "A simple wet etch for GaN," J. Electron. Mater. **28**(10), L24–L26 (1999).
[35]J. L. Weyher, J. Smalc-Koziorowska, M. Bańkowska, I. Dzięcielewski, Ł. Marona, and P. Perlin, "Photo-etching of GaN: Revealing nano-scale non-homogeneities," J. Cryst. Growth **426**, 153–158 (2015).
[36]C. Zhao, X. Zhang, C. W. Tang, J. Wang, and K. M. Lau, "Selective lateral photoelectrochemical wet etching of InGaN nanorods," J. Vacuum Sci. Technol. B **38**(6), 060602 (2020).
[37]H. Kawano, "Effective work functions of the elements: database, most probable value, previously recommended value, polycrystalline thermionic contrast, change at critical temperature, anisotropic dependence sequence, particle size dependence," Prog. Surf. Sci. **97**(1), 100583 (2022).
[38]P. G. Moses, M. Miao, Q. Yan, and C. G. Van de Walle, "Hybrid functional investigations of band gaps and band alignments for AlN, GaN, InN, and InGaN," J. Chem. Phys. **134**(8), 084703 (2011).
[39]M. Himmerlich, L. Lymperakis, R. Gutt, P. Lorenz, J. Neugebauer, and S. Krischok, "GaN(0001) surface states: Experimental and theoretical fingerprints to identify surface reconstructions," Phys. Rev. B **88**(12), 125304 (2013).
[40]Y. W. Chen and J. L. Kuo, "Density functional study of the first wetting layer on the GaN(0001) surface," J. Phys. Chem. C **117**(17), 8774–8783 (2013).
[41]L. C. A. Thompson and R. Pacer, "The solubility of indium hydroxide in acidic and basic media at 25 °C," J. Inorg. Nucl. Chem. **25**(8), 1041–1044 (1963).
[42]W. Guo, R. Kirste, I. Bryan, Z. Bryan, L. Hussey, P. Reddy, J. Tweedie, R. Collazo, and Z. Sitar, "KOH based selective wet chemical etching of AlN, AlxGa1−xN, and GaN crystals: A way towards substrate removal in deep ultraviolet-light emitting diode," Appl. Phys. Lett. **106**(8), 082110 (2015).

30 April 2024 15:54:17

Published under an exclusive license by AIP Publishing